Chemical Engineering Journal 498 (2024) 155480

Contents lists available at ScienceDirect

Chemical Engineering Journal

journal homepage: www.elsevier.com/locate/cej

Porous PU/PEDOT:PSS electrodes for probing bioelectricity in *Oscillatoria* sp. Cohorts

Francisco C. Cotta [a], Diogo Correia [a], Raquel Amaral [a], Felipe L. Bacellar [a], Damiano Duci [b], Luís Lopes [c], Luísa Cortes [d], Peter Zalar [e], Rupert Perkins [f], Paulo R.F. Rocha [a,*]

[a] *Bioelectronics & Bioenergy Research Lab, Centre for Functional Ecology-Science for People & the Planet, Associate Laboratory TERRA, Department of Life Sciences University of Coimbra, Coimbra 3000–456, Portugal*
[b] *Department of Architecture and Civil Engineering, University of Bath, Bath BA2 7AY, UK*
[c] *Laboratory of Instrumentation and Experimental Particle Physics, Coimbra 3000–456, Portugal*
[d] *Center for Neuroscience and Cell Biology (CNC) and Institute of Interdisciplinary Research of the University of Coimbra (III-UC), University of Coimbra, Rua Larga, Coimbra, Portugal*
[e] *Holst Centre/TNO, High Tech Campus 31, 5656AE, Eindhoven, the Netherlands*
[f] *School of Earth and Ocean Sciences, Cardiff University, Cardiff CF10 3AT, UK*

ARTICLE INFO

Keywords:
Porous PEDOT
PSS electrodes
Bioelectricity
Cyanobacteria
Paracrine signaling
Diffusion-limited noise

ABSTRACT

Increasing frequency of poor water quality events associated with cyanobacteria strains capable of producing taste and odour (T&O) metabolites and toxins is a global concern for human health and the drinking water industry. This is mostly due to the inability of timely detecting and predicting cyanobacteria productivity associated with water quality risks. Here, we develop and characterize an ultra-sensitive electrophysiology system based on porous polyurethane (PU) foams coated with poly (3, 4-ethylenedioxythiophene): polystyrene sulfonate (PEDOT: PSS) exploiting large-area electrodes of 199 cm^2, which maximizes the double-layer capacitance and concomitant detection sensitivity. The measured signal of the cyanobacteria model taxa *Oscillatoria* sp. results from the sum of all individual cell contributions and scales with electrode area, hence indicating correlation with productivity and biomass. Stochastic activity across the cohort is monitored as uncorrelated noise. Yet, when *Oscillatoria* sp. operate cooperatively, the signal appears as intercellular Ca^{2+} waves which are benchmarked with a conventional fluorescent probe and suppressed with the specific ion channel inhibitor gadolinium chloride. We suggest the existence of a paracrine signaling mechanism with Ca^{2+} acting as the chemical messenger across large cohorts that may prove to be linked with T&O metabolite 2-Methylisoborneol (2-MIB) production. The technology proposed here would enable *in-situ* real time monitoring of benthic cyanobacteria productivity and hence proxy data for their metabolite production. This paves the way for identifying sources of cyanobacteria metabolites including 2-MIB, geosmin and cyanotoxins, and hence identify intervention solutions and treatment optimization for removal of these detrimental metabolites.

1. Introduction

Cyanobacteria are the most diverse and widely distributed group of photosynthetic organisms [1]. An important socio-economic feature of cyanobacteria is their ability to produce secondary metabolites which may have negative effects, acting as toxins which adversely affect water and food or metabolites which significantly affect taste and odour quality, severely impacting on global aquaculture and drinking water suppliers, particularly the model organisms *Oscillatoria*, *Synechocystis* and *Cyanothece* [2–4]. The ability to timely detect cyanobacteria (e.g. increases in growth rate and biomass associated with harmful algal blooms and/or metabolite production) and to mechanistically understand how they adapt and thrive in different ecological niches is of high importance [5,6].

Currently, cyanobacterial taste and odour metabolites including 2-Methylisoborneol (MIB) and geosmin cost the UK Water Industry alone >£200 M a year. In water supply reservoirs monitoring of water chemistry and environmental parameters such as temperature of the water column or draw-off abstracted water, combined with functional genomics can give detailed analysis of planktonic cyanobacteria

* Corresponding author.
E-mail address: procha@uc.pt (P.R.F. Rocha).

https://doi.org/10.1016/j.cej.2024.155480
Received 21 May 2024; Received in revised form 26 August 2024; Accepted 2 September 2024
Available online 4 September 2024

producing the taste and odour (T&O) metabolite geosmin [2,3]. However, this sampling does not adequately give data on the benthic, sediment and reservoir periphery cyanobacterial community. An example is benthic cyanobacteria producing the T&O metabolite 2-MIB. This metabolite remains difficult and costly to remove in the water treatment works.

Membrane electricity, driven by ion movement across the cell membrane, has long been seen as a convertible energy currency for the cell, since early experiments with nerve cells at the onset of electrophysiology [7]. Surprisingly, studies reporting membrane electricity and concomitant function of cyanobacterial ion channels are scarce. Being procaryotes, ionic exchange and membrane potential should be controlled mainly through K^+/H^+ antiporters of the membrane [8]. Ca^{2+} has also been linked with the stress response of the model cyanobacteria *Synechocystis* either by its outward release through the mechanosensitive channel MscL in response to depolarization of the plasma membrane, or by acting in calcium-dependent potassium channels [9,10]. The existence of a low-frequency (1–2 s) community signaling has also been suggested in the late 80′s, using ethylrhodamine fluorescence as a probe for the transmembrane electrical potential, where filamentous cyanobacteria have been shown to propagate an electrical signal along trichomes of filamentous cyanobacteria [11].

Surprisingly, the electrical detection and bioelectrical conceptualization of procaryotes, particularly in cyanobacteria communities, hasn't been a common practice. Electrophysiology is instead commonly applied to neurons and performed through single cell methods such as patch clamp, or multi electrode arrays (MEAs), which generally comprise multiple planar electrodes, with areas below 50 μm^2, on an insulating substrate and in close contact with cells in aqueous media. The μm^2 sized planar electrodes measure the extracellular field potential, which contains a superposition of voltage gated, or ligand gated ion channels and intrinsic membrane fluctuations of one or few cells. MEAs are generally employed to record bioelectric events in the kHz regime with single-to-few cells resolution. To improve the measured signal quality bandpass filters are used and low-frequency biological oscillations are suppressed. Additionally, to obtain a good Signal-to-Noise Ratio (SNR), the electrode impedance should be as small as possible as compared to the amplifier input impedance, which is a challenge to achieve for conventional micrometre size plain electrodes [12], even with those made from, per instance, nanostructured Platinum, Platinum–Iridium [13,14] and Titanium Nitride [15], to name a few. Currently, a common practice to improve MEAs properties consists of coating the conventional metal electrodes with conducting polymers. Conducting polymers are functional materials with proven biocompatibility, good electrical and ionic conductivity and tunable chemical and mechanical properties [16]. Importantly, among the conducting polymers family, poly(3,4-ethylenedioxythiophene) polystyrene sulfonate (PEDOT:PSS) has demonstrated excellent biocompatibility [17], electrochemical stability [18], high (and tunable) [19], good charge transfer capability, excellent capacitive coupling and record-low interfacial impedance [20].

In MEAs, network events in action-potential producing cultures can be determined based on single cells activity across a multiple network of electrodes, typically comprising about 3000 electrodes/mm^2 [21]. While planar MEAs offer high spatial resolution, they are less favourable to detect collective synchronous activities across electrically quiescent cell networks, particularly in cases where a single cell size or filament is superior to the measuring electrode. In most cases, cells are plated and cultured on existing high density (HD) MEAs with cell densities around 3000 cells/mm^2 yielding about ~1 cell per electrode or less. Coordinated electrogenic events are therefore dispersed across the HD MEAs, hindering their cumulative electrical detection.

Here, we take a different approach from standard HD MEAs and develop ultra-large area electrodes to probe bioelectrical events from cohorts larger than ~10^4 cells/mm^2 on a single electrode. The breakthrough sensitivity is demonstrated by developing and rigorously characterizing three dimensional porous electrodes, based on a polyurethane (PU) substrate, dip coated with a champion material for electrophysiology e.g., poly(3,4-ethylenedioxythiophene) doped with polystyrene sulfonate (PEDOT:PSS) – owing to its biocompatibility, charge transfer ability, electrochemical stability, large capacitance and low impedance which promotes signal-to-noise ratio performance [22–30]. The extremely low impedance of PU/PEDOT:PSS electrodes allows for low frequency measurements of a model cyanobacteria, *Oscillatoria*, with an improved signal-to-noise ratio. For the first time, we detect and perform extracellular electrophysiology of whole *Oscillatoria* sp. cohorts adhered to PU/PEDOT:PSS porous electrodes. The measured signal results from the sum of all individual cell contributions and scales with electrode area. Stochastic activity across the cohort is monitored as uncorrelated noise. Yet, when *Oscillatoria* sp. operate cooperatively, the signal appears as synchronized Intercellular Ca^{2+} Waves (ICWs) which are effectively silenced using specific ion channels inhibitors. We conclude by suggesting the existence of a paracrine signaling mechanism with Ca^{2+} acting as the chemical messenger across *Oscillatoria* sp. cohorts. Findings have important applications regarding monitoring, predicting and quantifying cyanobacterial productivity and growth and could, through future work, be linked with secondary metabolite production, hence indicating highly applied applications within the water industry.

2. Materials and methods

2.1. Fabrication of porous electrodes

Commercially available polyurethane (PU) sponge (Eurospuma, 3049PR) were cut using a Gunville Foam Cutter, into a cylinder shape having 5.5 mm diameter and 2.5 mm height. PU cylinders were first cleaned with soap and distilled water, followed by sonication with acetone and distilled water for 10 min 1:1 (v/v), then dried with compressed air. PU cylinders were further cleaned and hydrophilized with oxygen plasma (Diener Atto, 40 kHz 200 W) for 10 min (Fig. 1A), which further improved attachment of the conducting polymer mixture to the PU. Then, PU cylinders were dip-coated in a poly(3,4-ethylenedioxythiophene) polystyrene sulfonate (PEDOT:PSS) mixture, prepared by mixing 19 mL of PEDOT:PSS (Clevios pH 1000, 94.25 vol% purchased from Heraeus Precious Metals GmbH & Co., Germany) with 80 μL (3-glycidyloxypropyl) trimethoxysilane, Sigma Aldrich, USA) in a proportion of 0.4:100 (v/v) and 1 mL of 5 % (v/v) dimethyl sulfoxide (DMSO, Sigma-Aldrich). The mixture was continuously stirred for 6 h at room temperature.

In the first dip-coating cycle, PU cylinders in the pristine state (PU only) were immersed into the PEDOT:PSS mixture, which from now on we refer to as PEDOT:PSS only and left overnight on an orbital shaker at 200 rpm (Fig. 1B). The dip-coated cylinders were then hot-baked at 120 ℃ in a muffle for 1 h (Fig. 1C), with the first 20 min inside a revolving grid at 0.4 rpm for an even distribution of the PEDOT:PSS mixture. The cylinders went through 4 coating cycles towards achieving a conductive coverage of the insulating polyurethane walls while maintaining the porosity and material integrity. In the 4th dip-coating cycle, the cylinder is placed on top of a thermally evaporated circular Au pad, with 10.7 mm^2 area. The metals are evaporated though a shadow mask using an Edwards High Vacuum 4P thermal evaporator and comprise a thin 10 nm layer of Ti and 50 nm of Au on a 2 mm thick borosilicate glass slide (purchased from Präzisions Glas & Optik GmbH, Germany) as described in previous works [28,30,31]. Fig. 1D illustrates the PU/PEDOT:PSS porous electrodes adhered on a circular Au electrode.

2.2. Electrical characterization of porous electrodes

The bulk conductivity of PEDOT:PSS was measured for spin coated thin films by the four-point probe van der Pauw method. A value of 520 S/cm was obtained, in close agreement with others [32]. Details are

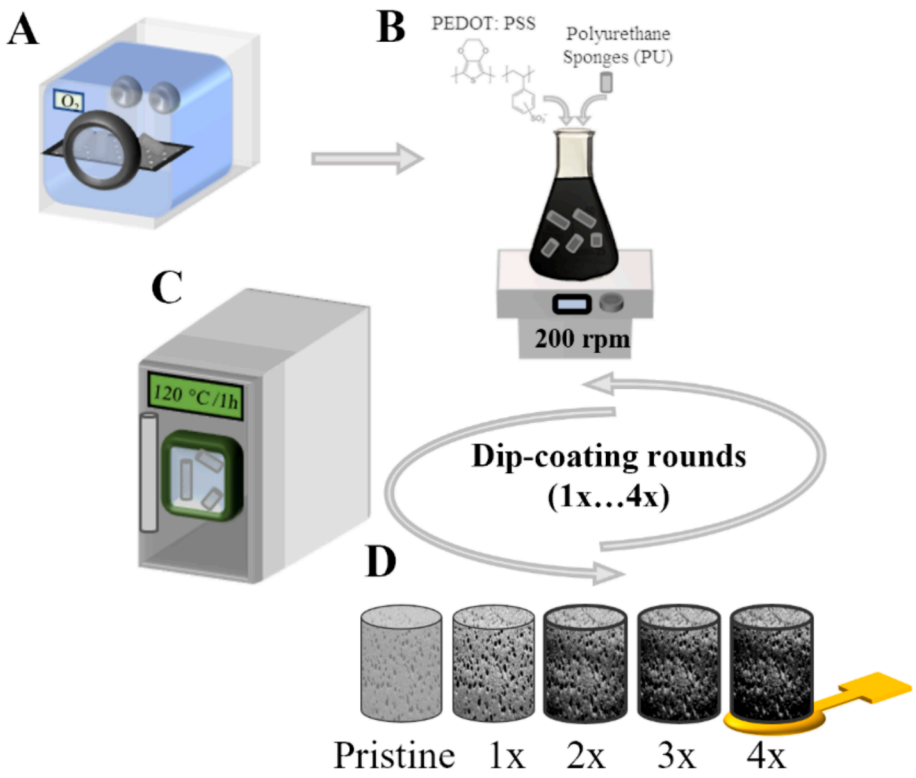

Fig. 1. Fabrication of the PU/PEDOT:PSS porous electrodes. (A) Cleaning and hydrophilization of the polyurethane pristine cylinder sponges with oxygen plasma prior to the dip-coating cycles; (B) immersion of PU sponges with PEDOT:PSS solution by stirring at 200 rpm overnight at RT; (C) hot baking at 120 °C for 1 h; (D) representation from 1 to 4 dip-coating cycles and attachment to the Au electrode pad.

presented in the Appendix B section 2. The conductivity of the porous electrodes was extracted from two-point probe I-V measurements on porous electrodes sandwiched between two copper electrodes. Details of the fabrication, such as the assembly of the electrodes, I-V measurements and determination of the contact resistance are presented in Appendix B section 3. The effectiveness of dip-coating cycles was assessed from systematic changes in the impedance. To this end Electrochemical Impedance Spectroscopy (EIS) measurements were performed on porous electrodes filled with an aqueous 100 mM KCl electrolyte. Details on the experimental set-up are presented in Appendix B section 4. The equivalent circuit and the extracted electrochemical parameters are presented in Appendix B section 5. The ultra-large surface area of porous PU/PEDOT:PSS electrodes means that more ions can adsorb onto the surface which, as discussed in Appendix B section 6, translates into measured volumetric capacitances in the order of the F/cm^3. Specifically, from the slope of the capacitance versus volume we derive a volumetric capacitance of 21.1F/cm^3. The piezoresistivity of PU/PEDOT:PSS electrodes shown in Appendix B section 7 was measured using a tensile tester (Mark-10, E303) outfitted with a 10 N load cell (Mark-10, MR03-2). The tensile tester loads and unloads the porous electrodes at a strain rate of 3.33 x 10^{-3} per second while recording the travel and applied force. Simultaneously, the resistance of the porous electrodes is measured using a source measure unit (Keithley 2612A) by applying a constant current of 1 mA.

2.3. Morphological characterization of porous electrodes

Cylinders of 1 mm height and 5.5 mm diameter were analysed, from pristine to 4x dip-coating cycles. The samples were prepared for scanning electronic microscopy (SEM) analysis by the deposition of a 10 nm thin metallization layer. For that purpose, the samples were placed inside a plasma generator Quorum SC7620 Mini Sputter Coater with a Glow Discharge System with a gold/palladium (Au/Pd) sputter target. The microstructural analysis was performed using a TESCAN VEGA 3 SBH Easy Probe SEM with a tungsten-heated cathode. The images were acquired with a working voltage of 5 kV and using the secondary electrons detector. Surface area of fabricated porous electrodes was determined by examining samples of 10 mm by the volumetric method with nitrogen with Brunauer-Emmett-Teller (BET) analysis (Micromeritics ASAP 2000 instrument) (n = 10). All samples were outgassed using heat and vacuum prior to analysis. Median pore diameter and porosity were determined by mercury porosimetry, (Micromeritics AutoPore IV 9500, Mercury Porosimeter). The instrument enables the intrusion of mercury into the porous structure of samples with a known dimension under controlled pressure. The samples were submitted to a pressure of 0.50 psi to 33,000 psi.

2.4. Maintenance of Oscillatoria sp

The *Oscillatoria* sp. UHCC 0332 was purchased from the HAMBI culture collection of the University of Helsinki, (https://www.helsinki.fi/hambi). The strain was cultivated in sterile BG11 medium (50x freshwater solution, Sigma), in a growth chamber (aralab, FC S600PL) with temperature 18 °C, photoperiod 12 h:12 h and light intensity 30 µmol/m^2/s^1 provided by cool white daylight fluorescent lamps. Healthy filaments were transferred to a Petri dish and reduced to smaller portions of ca. 3 mm long using a sterile scalpel. BG11 resistivity of 490 Ω cm was measured using a Multiparameter Pocket Meter ProfiLine Multi 3320 from WTW, Germany. A volume of 3 mL of the resulting cut out culture was seeded into the porous electrode which was previously cleaned with oxygen plasma (200 W and 10 min) followed washing three times with sterilized BG11 solution.

2.5. Extracellular electrophysiology and data analysis

Extracellular electrophysiology was performed using a low-noise

current amplifier (SR570, Stanford Research) with 5nA/V of gain and a dynamic signal analyser (35670A, Agilent) as in previous work [30]. Data were analysed in the time and frequency domain. The current noise spectra represent an average over 5 consecutive recordings. Statistical analysis of results was performed with a one tailed type 2 Student́s *t*-test, using MATLAB R2020b. The values found significantly different denote an effect of the treatment and are accompanied by the probability value of p, where $p < 0.05$ gives more than 95 % statistical confidence and $p < 0.10$ gives more than 90 % statistical confidence. The whole recording system was electrically isolated using a Faradaýs cage.

2.6. Functional screening and fluorescence imaging

A growing concentration of gadolinium chloride ($GdCl_3$) was prepared in culture medium and was added to the cells until few electrical spikes were observed. The medium was removed and replaced with 3 mL of $GdCl_3$ 200 μM, then replaced with 3 mL of $GdCl_3$ 400 μM and finally with 3 mL of $GdCl_3$ 800 μM. The cell suspension was then washed three times with culture medium and allowed to recover until electrical activity was restored. Cell viability was confirmed by microscopic inspection (Inverted microscope Zeiss Vert. A1) and with fluorescence though live/dead staining (LIVE/DEADTM BacLightTM kit Invitrogen; Zeiss AxioZoom.V16 with HXP 200c fluorescence unit).

For further determining the origin of the electrical signals, we performed a calcium flux assay to detect intracellular Ca^{2+} mobilization. In the case of filamentous cyanobacteria *Oscillatoria* sp., it can be anticipated to occur along the cells inside each filament (intra-filamentary) and among neighbour filaments (inter-filamentary). We used confluent agarized cultures of *Oscillatoria* sp. and incubated with the calcium-sensitive fluorescent dye Fluo4-AM (25 μM, Thermofisher), for 45 min in the dark, then washed in growth medium and observed under inverted Spinning Disc confocal microscope (Carl Zeiss, Jena). Images were acquired using the Plan-ApoChromat 20×/0.8 objective, an excitation of 488 nm and collected between 500 and 550 nm using the Evolve 512 EMCCD camera. The dye crosses the cell membrane, binds the calcium released from intracellular stores and its fluorescence intensity increases, directly correlated to an increase of the available Ca^{2+} in the cytoplasm. The images were analysed disregarding the autofluorescence channel.

3. Results and Discussion

3.1. PU/PEDOT:PSS electrode porosity is maintained and median pore size decreases with increasing number of dip-coating cycles

Conducting PU/PEDOT:PSS electrodes were fabricated based on 4 dip-coating cycles. SEM images were taken from pristine (PU only) to 4x dip-coating cycles (Fig. 2A to E). After the 1st cycle, the PEDOT:PSS was uniformly distributed through the internal sponge structure. We noticed that after 4 dip-coating cycles, at 5x, the original pore shape degrades and porosity decreases to 45 % (data not shown), possibly due to the degradation of solid polyurethane walls caused by DMSO used in preparing the PEDOT:PSS solution. Up to 4 dip-coating cycles the sponge morphology does not significantly change as seen by the photographs in Fig. 2A to E and dimension analysis as presented in Appendix B section 7.

An important aim for fabricating porous electrodes, particularly for measuring large cellular cohorts, is to maintain a large surface area upon dip coating, which is only possible if internal clogging doesn't occur. Indeed, the surface area of our porous electrodes is not significantly altered as a function of dip-coating cycles. On average the surface area changes only around 25 %, from a pristine mean surface area of 3.75 m^2/g to 2.83 m^2/g in PU/PEDOT:PSS electrodes with 4x dip-coating cycles (Table 1, Fig. 2F). The median pore diameter decreases due to PEDOT:PSS adherence to the pore walls. On average, we observed a 35 % change, from 219 μm to 143 μm in pore diameter (Table 1, Fig. 2G), This change is due to the increase of the thickness of the PEDOT:PSS film, which we estimate to be around 0.25 μm per dip-coating cycle (Table 1, Fig. 2I), extracted from SEM images of peeled PEDOT:PSS films induced by submerging the PU/PEDOT:PSS electrodes with 90 % ethanol under mechanical deformation. The porosity of PU/PEDOT: PSS electrodes as a function of dip-coating cycles was barely affected. On average we measure a decrease around 1–2 % per dip-coating cycle, varying from ~56 % in pristine samples, to ~52 % in 4x dip-coated electrodes. The percentage of PEDOT:PSS in a single porous electrode evolves from 1.1 % to 3.8 % as a function of dip-coating cycles from 1 to

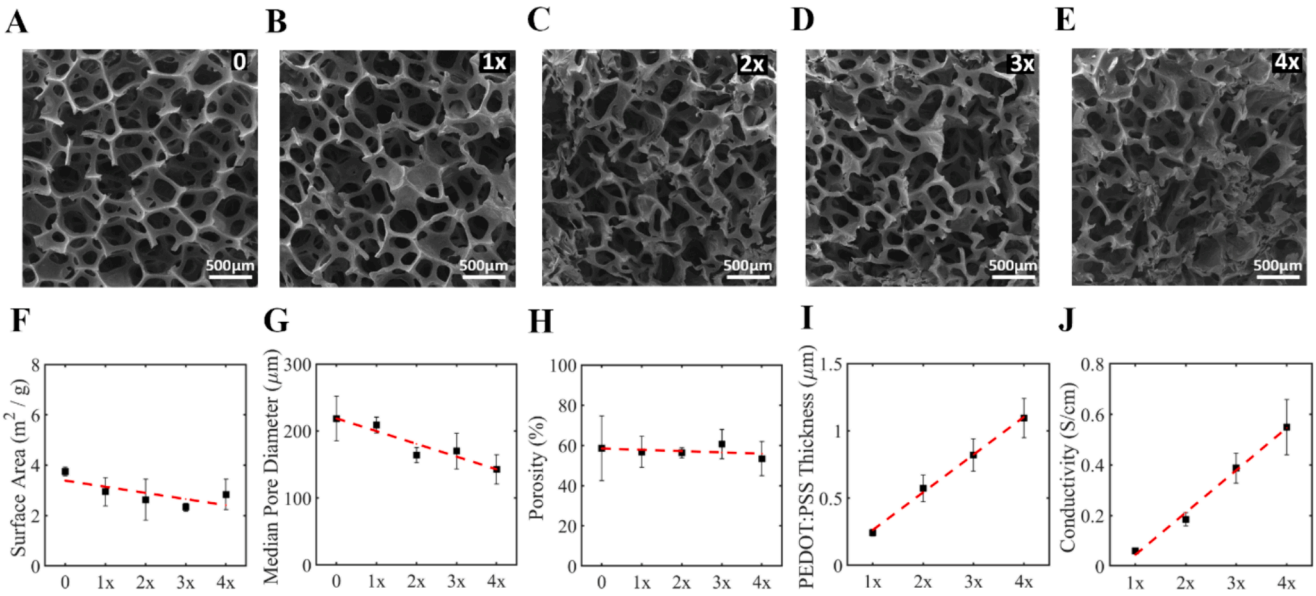

Fig. 2. Morphology characterization of PU/ PEDOT:PSS porous electrodes. (A to E) SEM images from pristine to 4x dip-coating cycles, (A) pristine; (B) after 1x; (C) after 2x; (D) after 3x and (E) after 4x, red dashed line shows a guide to the eye for each case; (F) surface area as a function of dip-coating cycles (n = 3); (G) median pore diameter as a function of dip-coating cycles; (H) porosity as a function of dip-coating cycles, (n = 3); (I) PEDOT:PSS thickness as a function of dip-coating cycles; (J) Conductivity as a function of dip-coating cycles. (For interpretation of the references to colour in this figure legend, the reader is referred to the web version of this article.)

Table 1
Morphological characterization of porous PU/PEDOT:PSS electrodes as a function of dip-coating cycles.

Coating Cycles	Surface Area (m^2/g)	Median Pore Diameter (μm)	Porosity (%)	PEDOT:PSS Thickness (μm)
Pristine (0)	3.75 ± 0.17	218.52 ± 33.30	58.58 ± 16.09	–
1x	2.94 ± 0.56	208.90 ± 11.96	56.81 ± 7.69	0.24 ± 0.02
2x	2.62 ± 0.81	163.86 ± 11.17	56.30 ± 2.54	0.57 ± 0.10
3x	2.33 ± 0.15	170.05 ± 26.74	60.65 ± 7.33	0.82 ± 0.11
4x	2.83 ± 0.60	142.76 ± 21.79	53.42 ± 8.49	1.09 ± 0.14

4x.

On porous materials, the electrical conductivity is strongly dependent on the PEDOT:PSS thickness which increases as a function of dip-coating cycles. Hence, we extracted the conductivity from two-point probe I-V measurements as a function of dip-coating cycles. The experimental setup, described in Appendix B section 3, consists of two parallel copper plates methodically connected with silver paste to the porous electrode surfaces, which enables reproducible I-V curves. The extracted conductivity values are presented in Fig. 2J. The first dip-coating cycle (1x) increases the sample conductivity to 0.06 ± 0.01 S/cm. The second (2x) dip-coating cycle reaches 0.18 ± 0.03 S/cm and the following coating cycles increases the conductivity by 0.16 S/cm per cycle. The conductivity reaches 0.55 ± 0.11 S/cm after 4 dip-coating cycles. We note these numbers are of course much lower than the bulk conductivity of PEDOT:PSS of 520 S/cm (Appendix B section 2). First of all, the conductivity is proportional to the PEDOT:PSS content. Table S3 shows that this content systematically increases with the number of coating cycles from about 1 % to 4 %. The maximum conductivity that can be expected when the PEDOT:PSS is uniformly distributed as a continuous slab is then about 5 to 20 S/cm. However, as the PEDOT:PSS in the pores is distributed not uniform but in a complicated RC network, a further reduction in the conductivity by some orders of magnitude can be expected.

The quality of the internal electrical PEDOT:PSS connections can be inferred from the pressure dependence of the conductivity. Upon applying pressure, the porous electrodes deform, and due to the shrinkage highly resistive percolating contacts can get shorted. The PU/PEDOT:PSS porous electrodes are indeed piezoresistive, meaning that the conductivity increases with pressure. However, as shown in Appendix B section 7, the effect is quite small. Application of a force of 5 N leads to just a 3 % decrease in electrode resistance, meaning that the PEDOT:PSS films in the porous electrodes are continuous.

In summary, dip coating of PU sponges with PEDOT:PSS leads to porous electrodes. The conductivity systematically increases with the number of coatings, while a high surface area and porosity is

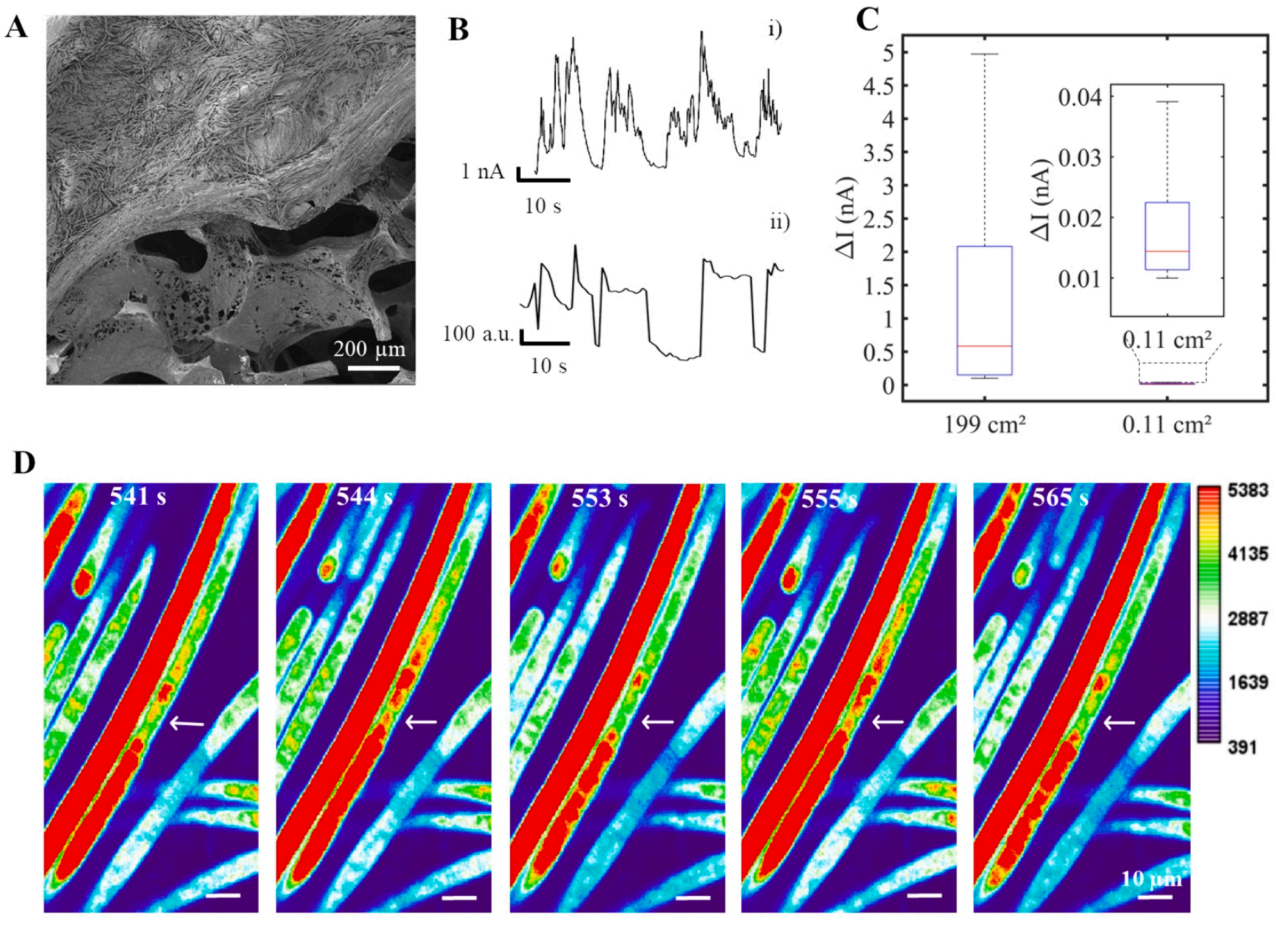

Fig. 3. Bioelectricity detected in *Oscillatoria* sp. cohorts. (A) SEM image of *Oscillatoria* sp. adhered to PU/PEDOT:PSS porous electrodes; (B) Example of fluctuations recorded in *Oscillatoria* sp. cohorts, in i) current over time recorded on PU/PEDOT:PSS porous electrodes and in ii) Ca^{2+} fluorescence intensity over time (see also full video recording in Appendix A); (C) Boxplot of the current magnitudes (ΔI corresponding to peak height) recorded in different electrode areas, 199 cm^2 (3D porous electrodes) and 0.11 cm^2 (Au planar electrode); (D) Time series of intra-filamentary Ca^{2+} fluctuations (region marked with arrows). The colour scale represents the a.u. intensity of Ca^{2+} detected by fluorescence.

maintained. The coating is uniformly spread across the whole internal porous structure leading to an ultra-low impedance and a high capacitance which scales linearly with volume. In fact, the ratio between the measured capacitance and surface area remains constant at 182.6 μF/cm^2 which corroborates with the view that the areal capacitance for PEDOT:PSS devices should be considered as a figure of merit [25,32].

3.2. *Oscillatoria sp. Signal amplitude scales with electrode area*

Oscillatoria species are known to have good adhesion properties and to form aggregates, as seen on rocks and other solid substrata and on the surface of benthic (bottom-water) sediments. Similarly, *Oscillatoria* sp. also adhere and proliferate inside and surrounding the PU/PEDOT:PSS porous electrodes and form aggregates as observed in SEM analysis depicted in Fig. 3A. We selected the 4x dip-coated PU/PEDOT:PSS electrode for extracellular electrophysiology due to the high porosity of 53.42 ± 8.49 % and good conductivity of 0.55 ± 0.11 S/cm. The surface area for the 4x dip-coated PU/PEDOT:PSS electrode can be calculated by multiplying the average weight of the PU/PEDOT:PSS cylinder (7.03 ± 0.05 mg) with the surface area determined in Fig. 2F, of 2.83 ± 0.60 cm^2, which gives an electrode surface area of 199.03 ± 1.44 cm^2.

The electrode layout is optimized to pick up long-timescale synchronized signals from a whole *Oscillatoria* sp. cohort. The sensor comprises two PU/PEDOT:PSS electrodes; one of the electrodes acts as measuring electrode and the other one as counter-electrode. The equivalent circuit shown in SI section 8 embodies the electrical coupling between the cell and the electrode similarly to previous works [27,28,30,33,34]. The parallel circuit network is formed by the charge transfer resistance, R_{ct}, and the Helmholtz-Gouy-Chapman double-layer capacitance, C_p, in series with the spreading resistance, R_{sol} that accounts for the signal loss into the surrounding electrolyte. A similar circuit describes the counter electrode. The electrical path from the sensing to the counter electrode has very high impedance, Z_{seal}, because of the large distance. We then amplify the cell current fluctuations, $i_{cyano}(t)$ using a transimpedance amplifier. The output voltage $v_0(t)$ is given by:

$$v_0(t) = -R_F i_s(t) \quad (1)$$

where R_F is the feedback resistance. The detected current can be approximated to:

$$i_{cyano}(t) \cong \frac{dv_s}{dt} \cdot C_p \left(1 - e^{\frac{-t}{R_{cleft} \cdot R_{ct}}}\right) \quad (2)$$

The measuring system allowed us to detect constantly occurring and functional, membrane capacitive current oscillations across large populations of *Oscillatoria* sp. strain. After 24 h of cell seeding, the *Oscillatoria* sp. cohort was well adhered to the porous electrode and generated current spikes (Fig. 3Bi). We noted that measured signals oscillated between asynchronous and bipolar signals with amplitudes from less than 20 pA to large magnitude quasi-periodic patterns reaching amplitudes above 5nA. The large magnitude spikes are likely due to synchronization across the whole cohort leading to superposition of all individual contributions. The interspike intervals suggests that the signals of the *Oscillatoria* sp. community become synchronized, implying their ability to sense and/or communicate as recently suggested in previous work [29]. To ascertain this is indeed the case, we quantified the measured amplitude in two well distinct cell densities. Since controlling the density of filamentous cyanobacteria is challenging, we compared the electrical spike magnitudes of the large PU/PEDOT:PSS porous electrodes with an active area of 199 cm^2 to the electrical spike magnitudes recorded with a smaller planar Au electrode with an active area of 0.11 cm^2. We also measured with SEM over 100 individual *Oscillatoria* sp. cells to calculate the average area of 6.84 ± 2.19 μm^2 per unit cell. Assuming a uniform cell coverage of the whole electrode area, we can estimate ~10^9 cells on the PU/PEDOT:PSS electrode against ~10^6 cells on the planar Au electrode.

The analysis in Fig. 3C represents two distinct replicates totalling 8580 spikes. The spike magnitude (ΔI) increases for larger areas, at least by a factor of 50 when considering the median magnitudes. The median magnitude displayed in the boxplot of Fig. 3C is 0.76nA for the large porous PU/PEDOT:PSS electrode. In the smaller planar Au electrode of 0.11 cm^2, the median amplitude found is 0.015nA. Hence, the signal emitted from *Oscillatoria* sp. cohorts scales with electrode area. Interestingly for both electrodes, quasi-periodic events are recorded, however with similar interspike intervals of about 5 s, indicating the existence of a slow and cooperative signaling mechanism across large *Oscillatoria* sp. cohorts nearly independent of electrode area.

The fluorescence assay showed that Ca^{2+} diffusion occurs inside each filament (intra-filamentary), from cell to cell in a progressive spatio-temporal pattern. The intra-filamentary Ca^{2+} diffusion occurs progressively along the filament and often in pulses of high and low intensity, with durations between 0.8 s (limited by instrumentation) to ~ 13 s, as demonstrated in Fig. 3D. From Fig. 3D and video recording in Appendix A, we noted that inter-filamentary Ca^{2+} flux is also likely occurring given the fluorescence increase in neighbouring filaments. The duration of intra- and inter-filamentary Ca^{2+} fluctuations are effectively similar and in very close agreement with the electric spikes detected in the PU/PEDOT:PSS sensor, as exemplified in Fig. 3Bii and i, respectively). Moreover, while gliding, we often noticed that when a highly fluorescent area of a filament approaches a non-fluorescent neighbour (within handover distance [29]), inter-filamentary communication likely occurred and provoked a Ca^{2+} increase within the neighbour filament, which typically occurs within less than 2 s (See video recording in Appendix A). Ca^{2+} flux is therefore very likely involved in the electrical communication events recorded from *Oscillatoria* sp. cohorts.

3.3. *Ca^{2+} mediates low-frequency current spikes across Oscillatoria sp. Cohorts*

Ca^{2+} has been linked with signaling of cyanobacteria, such as the *Synechocystis,* either by its outward release through the mechanosensitive channel MscL in response to depolarization of the plasma membrane or by acting in calcium-dependent potassium channels [9,10]. To ascertain that the measured current spikes are mediated by Ca^{2+} we used the calcium channel blocker $GdCl_3$. The blocker was tested in doubling concentrations from 200 to 800 μM.

Fig. 4A shows that $GdCl_3$ is able to suppress the electrical current spikes by over 90 % when using a concentration of 800 μM. In more detail, the basal spike rate of *Oscillatoria* after growing on the porous electrode surface for 3 weeks is on average 5 events/minute (Fig. 4B). The current spike rate slows down significantly ($p < 0.10$) after the addition of 200 μM $GdCl_3$ and slows further upon doubling the concentration to 400 μM, comparing to basal activity ($p < 0.10$), which was not enough to fully arrest the measured electrical spikes (>80 % of spike rate reduction). The spike rate reduces to near 0 upon adding a high concentration of 800 μM ($p < 0.05$). After washing out the blocker, the cells were allowed to recover and resumed electrical activity to a similar spike rate as the basal rate before the treatments, ca. 4 events/minute.

The basal electrical activity recorded in large *Oscillatoria* sp. cohorts in the time domain led to a current noise spectrum proportional to $1/f^{1.5}$, which is characteristic of a diffusion-limited noise [29,33,35,36]. The trend of γ in $1/f^{\gamma}$ decreases as a function of increasing $GdCl_3$ concentration, specifically from $1/f^{1.10}$ with 400 μM to $1/f^{0.77}$ with 800 μM, and back to $1/f^{1.5}$ after washout (inset Fig. 4C). We note that without cells, the current noise spectrum (shown in black symbols on Fig. 4C), had an almost linear $1/f^{0.5}$ pattern, and approached that of the cells under 800 μM of $GdCl_3$. The noise spectrum is nearly frequency independent while approaching to $4kT/R_{ct}$ where k is the Boltzmann constant and T is the absolute temperature, as modelled previously for planar electrodes [31].

The viability of *Oscillatoria* sp. on PU/PEDOT:PSS porous electrodes was assessed before and after adding $GdCl_3$, as shown in Fig. 4D and E,

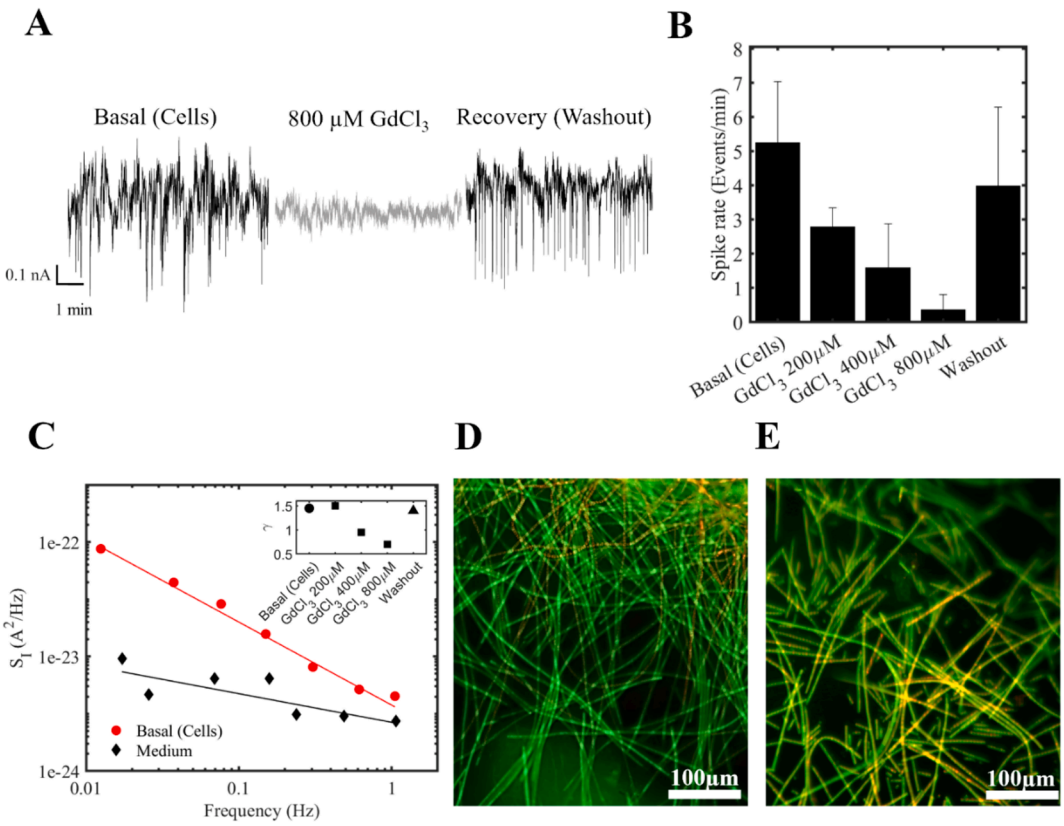

Fig. 4. Electrical activity and viability of *Oscillatoria* sp. on 3D porous electrodes. (A) electrical spikes before addition of ion blocker $GdCl_3$; blocking of spikes after addition of doubling concentrations of $GdCl_3$ 200, 400 and 800 µM; electrical spikes recorded after washing off the inhibitor showing resumed electrical activity; (B) Bar chart of spike rate, i.e. current spikes counted per minute, as a function of $GdCl_3$ concentration; (C) current noise spectra, S_I as a function of frequency. The noise spectra are average over 5 consecutive measurements. Red circles indicate cell activity and black diamonds indicate culture medium. The solid lines are calculated average. The inset shows γ variation of untreated cells, $GdCl_3$ treatments and recovery after washout; *Oscillatoria* sp. filaments stained with LIVE/DEAD ink, showing (D) most filaments alive (green) before $GdCl_3$ treatment and (E) most filaments alive with the presence of some dead filaments (red) and dead cells inside live filaments. (For interpretation of the references to colour in this figure legend, the reader is referred to the web version of this article.)

respectively. The stain is composed by two parts, the SYTO9 part which enters the membrane of healthy cells (green) and the propidium iodide which is membrane impermeable and DNA-binding, meaning that it reaches the DNA of disrupted membranes in dead cells and stains red. Before $GdCl_3$ treatment, most filaments are stained green in their full length. Most cells composing the filament had intact membranes and propidium iodide could not enter any of them (Fig. 4D). Yet, we did encounter a few red-stained filaments, possibly due to a finished life cycle, long before the staining (Fig. 4D).

The effect of adding $GdCl_3$ blocker with lower concentrations is known to be reversible where treated cells are capable of resuming electrical activity and metabolism. However, the effect of supressing electrical activity in *Oscillatoria* sp. was evident only with high concentration of 800 µM. Although most cells remain viable after adding 800 µM of $GdCl_3$, we did observe some cells with red staining, suggesting recent damage to membranes (Fig. 4E). This may indicate that in some cases, the disturbing of $GdCl_3$ to the membrane lipids neighbouring the Ca^{2+} channels was not reversible, and some permeation was available to propidium iodide. The hypothesis of some damaged channels corroborates with the slight decrease in spike rate before and after $GdCl_3$ treatment, from 5.26 ± 1.77 to 3.99 ± 2.30 events/minute as shown in Fig. 4B.

We hypothesize the linkage between cell signals and taste and odour metabolites due to the following mechanistic pathway. In cyanobacteria, ion fluxes exist across thylakoid membranes and contribute to respiration and regulation of photosynthesis [8]. Cyanobacterial photosynthesis results in measurable rates of electron transport that have been directly correlated with ATP production and Ca^{2+} ion efflux [9]. Photosynthetic proteins are known to be regulated by Ca^{2+}, in which calcium signalling is related to photosynthetic electron flow, in particular photosystem 1 electron transfer, and hence generation of the proton gradient responsible for ATP synthesis [37,38]. It is hence reasonable to link productivity and ion-driven cell signalling with ATP production. The second stage of the pathway is that taste and odour metabolite production by cyanobacteria has been shown to directly correlate with ATP production [39]. Taste and odour metabolites have long been reported to show close correlation with increased periods of productivity [2]. Hence, although further research is required, there is a reasonable pathway between electrogenic cell signalling and metabolite production.

4. Conclusions

PU/PEDOT:PSS porous electrodes were fabricated, modelled, and rigorously characterized for extracellular electrophysiology of large cell cohorts, up to ~10^4 cells/mm^2 or ~10^9 cells/electrode. Dip-coated PU/PEDOT:PSS electrodes maintain their porosity above 50 % and internal structure during four consecutive dip-coating cycles and increase in conductivity from 0.06 ± 0.01 S/cm to 0.55 ± 0.11 S/cm which corresponds to merely 1.1 % to 3.7 % of PEDOT:PSS coverage, with a ~0.2 µm thick PEDOT:PSS layer per cycle.

Our findings show that *Oscillatoria* sp. filaments adhere to and proliferate within the internal porous structure for over three weeks. Critically, by comparing the electrical signals obtained from large porous electrodes of 199 cm^2 with smaller electrodes of 0.11 cm^2, we ascertained that the electrical signalling scales at least by a factor of 50. The

large electrode area increases sensitivity and enables detection of *Oscillatoria* sp. over time. The current noise spectrum exhibits a $1/f^{1.5}$ frequency dependence historically attributed to a diffusion-limited process. Oscillations and diffusion of intra- and inter-filamentary Ca^{2+} are part of their basal activity, are here evidenced by fluorescence probing, and are likely due to paracrine cell–cell signalling. The signalling mechanism is related to Ca^{2+} ions as growing concentrations of the ion blocker $GdCl_3$, suppressed over 90 % of electrical activity.

Our analysis suggests that a chemical signal is released, detected, and transmitted by neighbouring cells, herewith propagating an ICW throughout the entire community. Future investigations aiming at identifying and functionally characterizing cyanobacteria ion channels are required to improve our understanding on membrane excitability and concomitant cyanobacteria ecophysiology. However, this study has clearly shown the potential to apply this technology to water quality sampling with regard to monitoring cyanobacterial productivity and biomass. The former has applications related to metabolite production associated with poor water quality, e.g. geosmin and 2-MIB associated with increased and sporadic patterns in productivity and the latter has applicability to prediction and monitoring of harmful algal blooms and associated problematic metabolite production. In particular the applicability to benthic cyanobacterial metabolite production will be of high interest to Water Companies globally.

CRediT authorship contribution statement

Francisco C. Cotta: Writing – original draft, Methodology, Investigation, Formal analysis, Data curation. **Diogo Correia:** Methodology, Investigation, Data curation. **Raquel Amaral:** Writing – review & editing, Writing – original draft, Methodology, Formal analysis, Data curation. **Felipe L. Bacellar:** Methodology, Formal analysis, Data curation. **Damiano Duci:** Methodology, Investigation. **Luís Lopes:** Methodology. **Luísa Cortes:** Methodology, Investigation. **Peter Zalar:** Writing – review & editing, Methodology, Investigation, Formal analysis. **Rupert Perkins:** Writing – review & editing, Investigation. **Paulo R.F. Rocha:** Writing – review & editing, Supervision, Project administration, Investigation, Funding acquisition, Formal analysis, Conceptualization.

Declaration of competing interest

The authors declare that they have no known competing financial interests or personal relationships that could have appeared to influence the work reported in this paper.

Data availability

All data are available in the main text and in Appendix A and B.

Acknowledgements

PRFR acknowledges the support and funding from the European Research Council (ERC) under the European Union's Horizon 2020 research and innovation programme [grant agreement No. 947897].

Appendix A. Supplementary material

Supplementary material to this article can be found online at https://doi.org/10.1016/j.cej.2024.155480.

References

[1] A. Sukenik, A. Kaplan, Cyanobacterial harmful algal blooms in aquatic ecosystems: A comprehensive outlook on current and emerging mitigation and control approaches, Microorganisms. 9 (2021) 1472, https://doi.org/10.3390/microorganisms9071472.

[2] R.G. Perkins, E.I. Slavin, T.M.C. Andrade, C. Blenkinsopp, P. Pearson, T. Froggatt, G. Godwin, J. Parslow, S. Hurley, R. Luckwell, D.J. Wain, Managing taste and odour metabolite production in drinking water reservoirs: The importance of ammonium as a key nutrient trigger, J. Environ. Manag. 244 (2019) 276–284, https://doi.org/10.1016/j.jenvman.2019.04.123.

[3] A.S. Hooper, P. Kille, S.E. Watson, S.R. Christofides, R.G. Perkins, The importance of nutrient ratios in determining elevations in geosmin synthase (geoA) and 2-MIB cyclase (mic) resulting in taste and odour events, Water Res. 232 (2023) 119693, https://doi.org/10.1016/j.watres.2023.119693.

[4] J. Pathak, P.K. Rajneesh, S.P. Maurya, D.P. Singh, Häder, R.P. Sinha, Cyanobacterial farming for environment friendly sustainable agriculture practices: Innovations and perspectives, Front. Environ. Sci. 6 (2018), https://doi.org/10.3389/fenvs.2018.00007.

[5] W.A.W. Mahari, W.A.W. Razali, K. Waiho, K.Y. Wong, S.S. Foo, A.S. Kamaruzzan, C.J.C. Derek, N.L. Ma, J. Chang, C. Dong, Y. Chisti, S.S. Lam, Light-emitting diodes (LEDs) for culturing microalgae and cyanobacteria, Chem. Eng. J. 485 (2024) 149619, https://doi.org/10.1016/j.cej.2024.149619.

[6] J. Pekkoh, K. Duangjan, K. Phinyo, T. Kaewkod, K. Ruangrit, T. Thurakit, C. Pumas, W. Pathom-aree, B. Cheirsilp, W. Gu, G. Wang, C. Chaichana, S. Srinuanpan, Turning waste CO_2 into value-added biorefinery co-products using cyanobacterium *Leptolyngbya* sp. KC45 as a highly efficient living photocatalyst, Chem. Eng. J. 460 (2023) 141765, https://doi.org/10.1016/j.cej.2023.141765.

[7] V.P. Skulachev, Membrane electricity as a convertible energy currency for the cell, Can. J. Biochem. 58 (1980) 161–175, https://doi.org/10.1139/o80-023.

[8] V. Checchetto, E. Teardo, L. Carraretto, E. Formentin, E. Bergantino, G. M. Giacometti, I. Szabo, Regulation of photosynthesis by ion channels in cyanobacteria and higher plants, Biophys. Chem. 182 (2013) 51–57, https://doi.org/10.1016/j.bpc.2013.06.006.

[9] L.V. Nazarenko, I.M. Andreev, A.A. Lyukevich, T.V. Pisareva, D.A. Los, Calcium release from *Synechocystis* cells induced by depolarization of the plasma membrane: MscL as an outward Ca^{2+} channel, Microbiology 149 (2003) 1147–1153, https://doi.org/10.1099/mic.0.26074-0.

[10] V. Checchetto, E. Formentin, L. Carraretto, A. Segalla, G.M. Giacometti, I. Szabo, E. Bergantino, Functional characterization and determination of the physiological role of a calcium-dependent potassium channel from cyanobacteria, Plant Physiol. 162 (2013) 953–964, https://doi.org/10.1104/pp.113.215129.

[11] I.I. Severina, V.P. Skulachev, D.B. Zorov, Coupling membranes as energy-transmitting cables. II. Cyanobacterial trichomes, J. Cell Biol. 107 (1988) 497–501, https://doi.org/10.1083/jcb.107.2.497.

[12] L. Bettamin, F. Mathieu, F. Marty, M.C. Blatche, D. Gonzalez-Dunia, E. Suberbielle, G. Larrieu, Real-time and high-resolution monitoring of neuronal electrical activity and pH variations based on the co-integration of nanoelectrodes and chem-FinFETs, Small 20 (2024) 1–11, https://doi.org/10.1002/smll.202309055.

[13] C. Boehler, T. Stieglitz, M. Asplund, Nanostructured platinum grass enables superior impedance reduction for neural microelectrodes, Biomaterials 67 (2015) 346–353, https://doi.org/10.1016/j.biomaterials.2015.07.036.

[14] A. Petrossians, J.J. Whalen III, J.D. Weiland, F. Mansfeld, Electrodeposition and characterization of thin-film platinum-iridium alloys for biological interfaces, J. Electrochem. Soc. 158 (2011) D269, https://doi.org/10.1149/1.3559477.

[15] S. Meijs, M. Fjorback, C. Jensen, S. Sørensen, K. Rechendorff, N.J.M. Rijkhoff, Electrochemical properties of titanium nitride nerve stimulation electrodes: An in vitro and in vivo study, Front. Neurosci. 9 (2015) 1–11, https://doi.org/10.3389/fnins.2015.00268.

[16] P. Zhang, J. Travas-Sejdic, Fabrication of conducting polymer microelectrodes and microstructures for bioelectronics, J. Mater. Chem. C 9 (2021) 9730–9760, https://doi.org/10.1039/d1tc01618k.

[17] M. Seiti, A. Giuri, C.E. Corcione, E. Ferraris, Advancements in tailoring PEDOT: PSS properties for bioelectronic applications: A comprehensive review, Biomater. Adv. 154 (2023) 213655, https://doi.org/10.1016/j.bioadv.2023.213655.

[18] S.M. Ajmal Mokhtar, E. Alvarez de Eulate, V. Sethumadhavan, M. Yamada, T. W. Prow, D.R. Evans, Electrochemical stability of PEDOT for wearable on-skin application, J. Appl. Polym. Sci. 138 (2021) 1–11, https://doi.org/10.1002/app.51314.

[19] M. Sanviti, A. Alegria, D.E. Martínez-Tong, Fabrication and nanoscale properties of PEDOT:PSS conducting polymer nanospheres, Soft Matter 18 (2022) 4554–4564, https://doi.org/10.1039/d1sm01712h.

[20] A. Wang, D. Jung, D. Lee, H. Wang, Impedance characterization and modeling of subcellular to micro-sized electrodes with varying materials and PEDOT:PSS coating for bioelectrical interfaces, ACS Appl. Electron. Mater. 3 (2021) 5226–5239, https://doi.org/10.1021/acsaelm.1c00687.

[21] X. Yuan, et al., Versatile live-cell activity analysis platform for characterization of neuronal dynamics at single-cell and network level, Nat. Commun. 11 (2020), https://doi.org/10.1038/s41467-020-18620-4.

[22] G. Dijk, A.L. Rutz, G.G. Malliaras, Stability of PEDOT:PSS-coated gold electrodes in cell culture conditions, Adv. Mater. Technol. 5 (2020) 1900662, https://doi.org/10.1002/admt.201900662.

[23] A. Elghajiji, X. Wang, S.D. Weston, G. Zeck, B. Hengerer, D. Tosh, P. Rocha, Electrochemical impedance spectroscopy as a tool for monitoring cell differentiation from floor plate progenitors to midbrain neurons in real time, Adv. Biol. 5 (2021) e2100330.

[24] S. Venkatraman, J. Hendricks, Z.A. King, A.J. Sereno, S. Richardson-Burns, D. Martin, J.M. Carmena, *In vitro* and *In Vivo* evaluation of PEDOT microelectrodes for neural stimulation and recording, IEEE Trans. Neural Syst. Rehabil. Eng. 19 (2011) 307–316, https://doi.org/10.1109/TNSRE.2011.2109399.

[25] C.M. Proctor, J. Rivnay, G.G. Malliaras, Understanding volumetric capacitance in conducting polymers, J. Polym. Sci. B 54 (2016) 1433–1436, https://doi.org/10.1002/polb.24038.
[26] E. Stavrinidou, P. Leleux, H. Rajaona, D. Khodagholy, J. Rivnay, M. Lindau, S. Sanaur, G.G. Maliaras, Direct measurement of ion mobility in a conducting polymer, Adv. Mater. 25 (2013) 4488–4493, https://doi.org/10.1002/adma.201301240.
[27] P.R.F. Rocha, A. Elghajiji, D. Tosh, Ultrasensitive system for electrophysiology of cancer cell populations: A review, Bioelectricity. 1 (2019) 131–138, https://doi.org/10.1089/bioe.2019.0020.
[28] M. Cabello, H. Ge, C. Aracil, D. Moschou, P. Estrela, J.M. Quero, S.I. Pascu, P. Rocha, Extracellular electrophysiology in the prostate cancer cell model PC-3, Sensors (Switzerland). 19 (2019) 1–11, https://doi.org/10.3390/s19010139.
[29] R. Amaral, D. Duci, F.C. Cotta, F.L. Bacellar, S. Oliveira, F. Verret, K. Asadi, L.K. J. Vandamme, N.M. Reis, L.D. Bryant, D. Tosh, J. Mouget, R. Perkins, P.R.F. Rocha, Ion-driven communication and acclimation strategies in microalgae, Chem. Eng. J. 473 (2023) 144985, https://doi.org/10.1016/j.cej.2023.144985.
[30] M. Ribeiro, A. Elghajiji, S.P. Fraser, Z.D. Burke, D. Tosh, M.B.A. Djamgoz, P. Rocha, Human breast cancer cells demonstrate electrical excitability, Front. Neurosci. 14 (2020) 1–10, https://doi.org/10.3389/fnins.2020.00404.
[31] P.R.F. Rocha, P. Schlett, U. Kintzel, V. Mailander, L.K.J. Vandamme, G. Zeck, H. L. Gomes, F. Biscarini, D.M. de Leeuw, Electrochemical noise and impedance of Au electrode/electrolyte interfaces enabling extracellular detection of glioma cell populations, Sci. Rep. 6 (2016) 34843, https://doi.org/10.1038/srep34843.
[32] M. Bianchi, S. Carli, M.D. Lauro, M. Prato, M. Murgia, L. Fadiga, F. Biscarini, Scaling of capacitance of PEDOT:PSS: Volume Vs. Area, J. Mater. Chem. C. 8 (2020) 11252–11262, https://doi.org/10.1039/d0tc00992j.
[33] P.R.F. Rocha, A.D. Silva, L. Godinho, W. Dane, P. Estrela, L.K.J. Vandamme, J. B. Pereira-Leal, D.M. de Leeuw, R.B. Leite, Collective electrical oscillations of a diatom population induced by dark stress, Sci. Rep. 8 (2018) 1–8, https://doi.org/10.1038/s41598-018-23928-9.
[34] M.C.R. Medeiros, A. Mestre, P. Inácio, S. Asgarif, I.M. Araújo, P.C. Hubbard, Z. Velez, M.L. Cancela, P.R.F. Rocha, D.M. de Leeuw, F. Biscarini, H.L. Gomes, An electrical method to measure low-frequency collective and synchronized cell activity using extracellular electrodes, Sens. Bio-Sens. Res. 10 (2016) 1–8, https://doi.org/10.1016/j.sbsr.2016.06.002.
[35] P.R.F. Rocha, H.L. Gomes, L.K.J. Vandamme, Q. Chen, A. Kiazadeh, D.M. de Leeuw, S.C.J. Meskers, Low-frequency diffusion noise in resistive-switching memories based on metal-oxide polymer structure, IEEE Trans. Electron Devices 59 (2012) 2483–2487, https://doi.org/10.1109/TED.2012.2204059.
[36] P.R.F. Rocha, H.L. Gomes, K. Asadi, I. Katsouras, B. Bory, F. Verbakel, P. van de Weijer, D.M. de Leeuw, S.C.J. Meskers, Sudden death of organic light-emitting diodes, Org. Electron. 20 (2015) 89–96, https://doi.org/10.1016/j.orgel.2015.02.009.
[37] Q. Wang, S. Yang, S. Wan, X. Li, The significance of calcium in photosynthesis, Int. J. Mol. Sci. 20 (2019) 1–14, https://doi.org/10.3390/ijms20061353.
[38] M. Białasek, M. Górecka, R. Mittler, S. Karpiński, Evidence for the involvement of electrical, calcium and ROS signaling in the systemic regulation of non-photochemical quenching and photosynthesis, Plant Cell Physiol. 58 (2017) 207–215, https://doi.org/10.1093/pcp/pcw232.
[39] M. Behr, et al., Description of the mechanisms underlying geosmin production in Penicillium expansum using proteomics, J. Proteomics 96 (2014) 13–28, https://doi.org/10.1016/j.jprot.2013.10.034.